AUT Journal of Mathematics and Computing

AUT J. Math. Comput., 6(3) (2025) 193-203
https://doi.org/10.22060/AJMC.2023.22640.1182

Original Article

# A new central-upwind scheme for solving the shallow water equations

Rooholah Abedian*

*School of Engineering Science, College of Engineering, University of Tehran, Iran*

**ABSTRACT:** We have conducted a study where we applied one-dimensional central-upwind methods to estimate solutions of the Saint-Venant (SV) system. Our approach carefully considers the source terms associated with bottom topography. Within the context of the SV system, there are steady-state solutions that arise when the non-zero gradients of flux are exactly balanced by the corresponding source terms. Maintaining this delicate equilibrium with numerical approaches presents a challenging problem. Finding slight variations in these states proves to be extremely difficult in the field of computing. To address this, we propose an extension of semi-discrete central schemes, commonly employed in hyperbolic conservation law systems, to encompass balance laws (BL). In our approach, we specifically focus on discretizing the source term with great care and attention. To verify the superior accuracy, precise preservation of the C-property, and outstanding resolution of our approach, we perform comprehensive one-dimensional simulations on both continuous and discontinuous solutions.

**Review History:**
Received:30 August 2023
Revised:20 November 2023
Accepted:09 December 2023
Available Online:01 July 2025

**Keywords:**
Saint-Venant system
Central-upwind methods
Balance laws
Hyperbolic conservation laws

**MSC (2020):**
65M06; 35L65

## 1. Introduction

The Saint-Venant system is a commonly employed model that is extensively utilized to simulate fluid flows in river and coastal environments. It describes the dynamics of fluid flow by employing a formulation based on conservation laws, while also incorporating an additional term to account for external influences. In one spatial dimension, the Saint-Venant system is expressed as follows:

$$\begin{cases} h_t + (hv)_x = 0, \\ (hv)_t + \left(hv^2 + \frac{1}{2}gh^2\right)_x = -ghz_x, \end{cases} \tag{1}$$

In this particular formulation, the variables are defined as follows: $z(x)$ represents the elevation of the river or coastal bottom at position $x$, $h$ represents the depth of the fluid above the bottom at position $x$ and time $t$, $v$ denotes the average velocity of the fluid in the vertical direction at position $x$ and time $t$, and $g$ represents the gravitational constant.

*Corresponding author.
*E-mail addresses:* rabedian@ut.ac.ir

Similar to other systems governed by balance laws, the SV system also exhibits steady-state solutions in which the existence of non-zero gradients of flux is exactly balanced by the source terms. Numerically capturing these steady-state solutions, as well as their perturbations, poses significant challenges. In general, conventional numerical methods for solving conservation laws face challenges in accurately preserving the intricate balance between the fluxes and the source terms.

A scheme which preserves stationary steady-states was proposed by LeVeque [16]. This approach involves proposing a Riemann problem at the centre of each grid cell in such a way that the difference in flux precisely offsets the source term. To determine the updated averaged values for the half-cells, it is necessary to solve a non-linear algebraic problem. LeVeque demonstrated in [16] that there are instances where his iterative method fails to converge. Gallouët et al. pursued a distinct approach, although one that still relies on intricate Riemann problem solvers, as described in [9]. Extensive research has demonstrated that kinetic schemes possess the ability to preserve non-negative water height, maintain stationary steady-states, and satisfy an entropy inequality. Perthame et al. (2000) introduced first-order kinetic solvers according to [6]. High-order kinetic methods, despite their relatively complicated form, may only fulfil a subset of these properties. The problem discussed in the paper [21] was addressed by the authors using the essentially non-oscillatory (ENO) and weighted ENO (WENO) schemes. In their study, the authors applied the weighted essentially non-oscillatory method not just to the flow, but also to a merged entity consisting of the flow and the source component. To explore similar studies, please refer to [18, 19, 22, 23].

In this paper, we introduce a new fourth-order central-upwind method for the SV system. Our approach builds upon the method proposed in [1] for solving the Hamilton-Jacobi equations. Significant emphasis is placed on carefully discretizing the source term with meticulous attention, with the objective of accurately reproducing the differential properties at the numerical level and preserving steady-state solutions that remain unchanged over time.

Lately, there has been a notable surge of interest in central schemes for solving hyperbolic conservation laws, owing to their simplicity, efficiency, and robustness. The Godunov-type schemes utilized in these methods rely on precisely evolving an approximate piecewise polynomial reconstruction. They do not necessitate the use of (approximate) Riemann problem solvers and, as a result, can serve as versatile black-box solvers for a wide range of problems. The initial central scheme prototype is known as the first-order Lax-Friedrichs scheme, as documented by Friedrichs and Lax in their work [8]. Nessyahu and Tadmor introduced the 1D generalization of the Lax-Friedrichs method, known as NT scheme, in their paper cited as [17]. The second-order NT scheme is staggered. It is worth noting that these methods do not maintain the preservation of stationary steady-states.

One notable disadvantage of staggered central methods is their tendency to exhibit relatively high numerical dissipation. This dissipation becomes more pronounced when $\Delta t$ (time step) is significantly smaller than $\Delta x$ (spatial scale) and forced to be so. A similar issue arises when calculating the solution for extended periods, such as in steady-state calculations. Authors of [15] proposed a novel category of semi-discrete central methods that exhibit significantly reduced numerical dissipation. This is accomplished by utilizing *local* propagation speeds to obtain a more accurate estimation of the width of the Riemann fans. However, it is important to note that their approach does not involve any effort to solve Riemann problems. The proposal in [10] introduced the third-level expansion of these approaches, while their authentic multidimensional advancement was formulated in [14]. By taking into account the local speeds that are specifically oriented towards *one side*, it is possible to achieve even greater reduction in numerical dissipation. As a consequence, the central-upwind schemes [12, 13] are obtained.

The paper is structured as follows: Section 2 provides an introduction to the numerical method employed for balance laws.The paper includes the presentation of results from various one-dimensional simulations in Section 3, followed by concluding remarks in Section 4.

## 2. A new fourth-order central-upwind methods for BL

In this section, the specifics of developing the novel approach for the 1D SV system will be presented.

### *2.1. Notations and preliminaries*

We begin by addressing the broader issue of approximating solutions for 1D systems of BL, which can be represented as follows:

$$u_t + f(u)_x = S(u, x, t), \tag{2}$$

where $u$ is a vector in $\mathbb{R}^N$. These equations are subject to the initial condition $u(x, 0) = u_0(x)$. To keep things simple, we employ a evenly spaced spatial grid denoted by $x_\alpha := \alpha\Delta x$, although the proposed scheme in this research work can be extended to non-uniform spatial grid as well. We use the term $\bar{u}_j(t)$ to represent the average

value of $u(x,t)$ within the interval $I_j = [x_{j-1/2}, x_{j+1/2}]$. Mathematically, the average value $\bar{u}_j(t)$ is defined as:

$$\bar{u}_j(t) := \frac{1}{\Delta x}\int_{I_j} u(x,t)dx,$$

where $\Delta x$ represents the width of the interval $I_j$ and the integral is taken over that interval. In the context of one-dimensional (1D) scenarios, an alternative representation of Eq. (2) can be expressed using average values within cells. This can be written as:

$$\frac{d}{dt}\bar{u}_j(t) + \frac{f(u(x_{j+1/2},t)) - f(u(x_{j-1/2},t))}{\Delta x} = \frac{1}{\Delta x}\int_{I_j} S(u,x,t)dx. \tag{3}$$

By employing an appropriate quadrature method for the integral over the spatial domain on the right-hand side of (3), and estimating $f(u(x,t))$ at the grid points located at half-integer positions, denoted as $x = x_{j\pm1/2}$, a semi-discrete scheme is derived. The semi-discrete scheme, known as the "central-upwind" method, includes an extra term to incorporate the influence of the source term. It can be expressed as follows:

$$\frac{d}{dt}\bar{u}_j(t) = -\frac{H_{j+1/2}(t) - H_{j-1/2}(t)}{\Delta x} + \bar{S}_j(t), \tag{4}$$

where the numerical fluxes, denoted as $H_{j+1/2}(t)$, are provided by [12]

$$H_{j+1/2}(t) := \frac{a^+_{j+1/2}f(u^-_{j+1/2}) - a^-_{j+1/2}f(u^+_{j+1/2})}{a^+_{j+1/2} - a^-_{j+1/2}} + \frac{a^+_{j+1/2}a^-_{j+1/2}}{a^+_{j+1/2} - a^-_{j+1/2}}\left(u^+_{j+1/2} - u^-_{j+1/2}\right). \tag{5}$$

Within this particular framework, the expressions $u^+_{j+1/2} := R_{j+1}(x_{j+1/2},t)$ and $u^-_{j+1/2} := R_j(x_{j+1/2},t)$ signify the values on the right and left sides, respectively, at the location $x = x_{j+1/2}$. These values correspond to a polynomial interpolation that is both conservative and free from oscillations, and are evaluated using the function $R$. This interpolant, denoted as $\tilde{u}(x,t)$, can be expressed as a summation over $j$ of $R_j(x,t)\chi_j$, where $\bar{u}_j(t)$ denotes the previously computed cell averages used for reconstruction at each time step. The polynomials $\{R_j(.,t)\}$ are specified degree functions, and $\chi_j$ represents the characteristic function of $I_j$. Special attention will be given to $\bar{S}_j(t)$, and it will be addressed in a later discussion. The determination of the one-sided "local" propagation speeds, denoted as $a^{\pm}_{j+1/2}$, is achieved through the following equations:

$$\begin{aligned} a^+_{j+1/2} &= \max\left\{\lambda_N\left(\frac{\partial f}{\partial u}(u^-_{j+1/2})\right), \lambda_N\left(\frac{\partial f}{\partial u}(u^+_{j+1/2})\right), 0\right\}, \\ a^-_{j+1/2} &= \min\left\{\lambda_1\left(\frac{\partial f}{\partial u}(u^-_{j+1/2})\right), \lambda_1\left(\frac{\partial f}{\partial u}(u^+_{j+1/2})\right), 0\right\}. \end{aligned} \tag{6}$$

Here, $\lambda_1 < \cdots < \lambda_N$ represents the $N$ eigenvalues of the Jacobian $\dfrac{\partial f}{\partial u}$.

**Remark 2.1.** *It is important to highlight that the simplicity of the suggested method is a key benefit. Specifically, the 1D system of BL can be tackled by solving its components separately, without the need for (approximate) Riemann problem solvers.*

**Remark 2.2.** *In this section, a semi-discrete approach is described, and therefore the equation (4) establishes a set of ordinary differential equations (ODEs). In order to solve this system effectively, it is essential to utilize an ODE solver that is both stable and possesses an appropriate order. To demonstrate our numerical examples, we employed the third-order strong stability-preserving (SSP) Runge-Kutta solver proposed by Shu et al. [20]. The solver, described by the following equations, was utilized:*

$$\begin{aligned} u^{(1)}_j &= u^n_j + \Delta t F(u^n_j), \\ u^{(2)}_j &= \tfrac{3}{4}u^n_j + \tfrac{1}{4}u^{(1)}_j + \tfrac{1}{4}\Delta t F(u^{(1)}_j), \\ u^{n+1}_j &= \tfrac{1}{3}u^n_j + \tfrac{2}{3}u^{(2)}_j + \tfrac{2}{3}\Delta t F(u^{(2)}_j), \end{aligned} \tag{7}$$

*where $F$ represents the right-hand side of equation (4).*

### 2.2. Non-oscillatory piecewise polynomial reconstructions

In order to generate a central-upwind method of a particular degree, it is essential to utilize a segmented polynomial reconstruction, which is referred to as $R_j$, with an appropriate level of complexity. In the subsequent numerical simulations, we utilize a segmented reconstruction of fourth-order, which can be described as follows. An option that can be explored involves the utilization of an essentially non-oscillatory (ENO) reconstruction technique. By combining interpolants obtained from different stencils using a convex combination, the polynomial order is effectively decreased. As a consequence, the Weighted Essentially Non-Oscillatory (WENO) interpolants are derived [5, 4, 3].

In order to obtain a reconstruction that is essentially non-oscillatory, it is necessary to introduce three additional polynomials denoted as $R_l(x)$, where $l = -1, 0, 1$. These polynomials are used to approximate the function $u(x)$ with a lower degree of accuracy on the interval $I_j$. Consequently, the polynomial $R_l(x)$, which achieves second-order accuracy, is defined on the reduced stencil comprising the intervals $\{I_{j-1+l}, I_{j+l}, I_{j+1+l}\}$. The construction of each of these polynomials involves formulating the following interpolation conditions:

$$\frac{1}{\Delta x}\int_{I_{j-m+l}} R_l(x)dx = \bar{u}_{j-m+l}, \qquad m = -1, 0, 1, \quad l = -1, 0, 1. \tag{8}$$

Given that $\deg(R_l(x)) \leq 2$ for $l = -1, 0, 1$, it is possible to express $R_l(x)$ as the sum of terms from $m = 0$ to $m = 2$, where each term is represented by $\frac{a_m^l}{m!}(\frac{x-x_j}{\Delta x})^m$. The coefficients for $R_{-1}(x)$ and $R_0(x)$, arranged from left to right, are as follows:

$$\begin{cases} a_0^{-1} = \frac{-1}{24}(\bar{u}_{j-2}^n - 2\bar{u}_{j-1}^n - 23\bar{u}_j^n), \\ a_1^{-1} = \frac{1}{2}(\bar{u}_{j-2}^n - 4\bar{u}_{j-1}^n + 3\bar{u}_j^n), \\ a_2^{-1} = \bar{u}_{j-2}^n - 2\bar{u}_{j-1}^n + \bar{u}_j^n, \end{cases} \qquad \begin{cases} a_0^0 = \frac{1}{24}(23\bar{u}_j^n + 2\bar{u}_{j+1}^n - \bar{u}_{j+2}^n), \\ a_1^0 = -\frac{1}{2}(6\bar{u}_j^n - 4\bar{u}_{j+1}^n - \bar{u}_{j+2}^n), \\ a_2^0 = \bar{u}_j^n - 2\bar{u}_{j+1}^n + \bar{u}_{j+2}^n. \end{cases}$$

And for $R_1(x)$, the coefficients are

$$\begin{cases} a_0^1 = \frac{-1}{24}(\bar{u}_{j-1}^n - 26\bar{u}_j^n + \bar{u}_{j+1}^n), \\ a_1^1 = \frac{-1}{2}(\bar{u}_{j-1}^n - \bar{u}_{j+1}^n), \\ a_2^1 = \bar{u}_{j-1}^n - 2\bar{u}_j^n + \bar{u}_{j+1}^n. \end{cases}$$

The reconstruction is generated by taking into account a convex combination of the aforementioned polynomials,

$$R_j(x) = \sum_{l=-1}^{1} w_l R_l(x), \qquad w_l \geq 0, \qquad \sum_l w_l = 1. \tag{9}$$

In regions of smoothness, the coefficients $w_l$ of the convex combination in (9) are selected to ensure the highest achievable accuracy. However, when a discontinuity is present, these coefficients are automatically adjusted to utilize the most favourable one-sided stencil, which produces the least amount of oscillations in the reconstruction. In accordance with the symbols used in [5], the weights $w_l$ are expressed as follows:

$$w_l = \frac{\alpha_l}{\sum_{m=-1}^{1} \alpha_m}, \qquad \alpha_l = \frac{C_l}{(\epsilon + IS_l)^2}, \qquad l = -1, 0, 1. \tag{10}$$

The value of the constant $\epsilon$ is chosen empirically as $\epsilon = 10^{-6}$ to ensure that the denominator does not become zero. Furthermore, the smoothness indicators, $IS_l$, are determined as

$$IS_l = \sum_{m=1}^{2} \int_{I_j} \Delta x^{2m-1} \big(R_l^{(m)}(x)\big)^2 dx. \tag{11}$$

The smoothness indicator swaps the linear weights to non-linear weights, to certify both accuracy in smooth areas and non-oscillatory performance when there is at least one small stencil contains discontinuities.

Performing an explicit integration yields the following result:

$$IS_l = a_1^2 + \frac{13}{12}a_2^2, \qquad l = -1, 0, 1.$$

The properties of the numerical stencil remain unchanged regardless of the selection of the constants $C_l$. $R_j(x)$ achieves the desired accuracy regardless of the specific choice of symmetric constants. For more detailed information, please refer to [2].

### 2.3. Source term integration over spatial domain

To attain fourth-order accuracy in the temporal domain, the utilization of Simpson's quadrature rule is employed. The integration needs to be carried out at time $t^n$. The primary objectives of this process are to attain high-order accuracy and ensure proper balancing. We represent the water's surface at a specific moment as $\eta$, defined as the sum of $h$ and $z$ ($\eta := h + z$). By recognizing that $\eta$, rather than $h$, needs to stay constant when examining stationary solutions, Eq. (1) can be expressed using $\eta$ and the momentum $hv$. Given that the bottom topography $z(x)$ remains unchanged over time, we have [11]

$$\begin{cases} \eta_t + (hv)_x = 0, \\ (hv)_t + \left( \dfrac{(hv)^2}{\eta - z} + \frac{1}{2} g(\eta - z)^2 \right)_x = -g(\eta - z) z_x. \end{cases} \tag{12}$$

Then, we have

$$\begin{aligned} \bar{S}_j^{(2)}(t) &= \frac{1}{\Delta x} \int_{x_{j-1/2}}^{x_{j+1/2}} g(z - \eta) z_x dx \\ &\approx \frac{g}{6} \Big( (z_{j+1/2} - \eta_{j+1/2}^-)(z_x)_{j+1/2}^- + 4(z_j - \eta_j)(z_x)_j + (z_{j-1/2} - \eta_{j-1/2}^+)(z_x)_{j-1/2}^+ \Big). \end{aligned} \tag{13}$$

To compute the value of the free-surface level $\eta$, which is the first component of the vector $u = (\eta, hv)^T$, at the grid points $x_{j\pm1/2}$ as required in (13), we utilize $\eta_{j\pm1/2}^{\mp} = R_j(x_{j\pm1/2})$. In this context, the function $R_j(x)$ refers to a non-oscillatory piecewise polynomial reconstruction method, which is obtained using an equation that is identical to (9). To compute the bottom slope $z_x$ at the grid points $x_j$, a modified approach is employed. This modification is based on adapting the reconstruction of flux derivative point-values, which was originally introduced in the classical central WENO scheme (as described in subsection 2.2). If we define $T(x)$ as the reconstruction of $z(x)$ using the expression $T(x) = \sum_j P_j(x)\chi_j$, then the approximation for the bottom slope $z_x$ can be represented by $T'(x)$. We will examine three polynomials, denoted as $P_l(x)$, each with a degree of 2. These polynomials are associated with the stencils $\{I_{j-1+l}, I_{j+l}, I_{j+1+l}\}$. The coefficients of these polynomials, $P_l(x)$, are uniquely determined by ensuring that $P_l(x)$ passes through the three-point values of $z(x)$, which are computed at the cell centres of the corresponding stencils. This can be expressed as follows:

$$P_l(x_{j-m+l}) = z(x_{j-m+l}), \quad l = -1, 0, 1, \quad m = -1, 0, 1. \tag{14}$$

The function $P_j(x)$ can be represented as a linear combination of the three functions $P_l(x)$, where the coefficients or weights associated with each polynomial are denoted as $w_l$. This combination ensures that the resulting polynomial is convex (refer to Eq. (9)). These weights are calculated using Eq. (10), which employs a symmetric set of linear weights. The corresponding $IS_l$ values are determined by evaluating Eq. (11), where $P_l(x)$ is obtained by using the point values of the function $z(x)$. By following this procedure, a fourth-order reconstruction is achieved. As a result, we obtain the following relationships:

$$(z_x)_{j\pm1/2}^{\mp} = T_j'(x_{j\pm1/2}), \qquad (z_x)_j = T_j'(x_j). \tag{15}$$

Here, $(z_x)_{j\pm1/2}^{\mp}$ represents the bottom slopes computed at the cell interfaces, while $(z_x)_j$ corresponds to the bottom slope evaluated at the cell centre. These values are determined based on the derivative of the reconstructed polynomial $T_j(x)$.

## 3. 1D numerical results

This section demonstrates the effectiveness of our central-upwind method by providing several 1D examples for testing purposes. The value assigned to the gravitational constant $g$ is 9.812 $m/s^2$. In the majority of cases, the CFL constant is selected in a way that fulfils the hyperbolic CFL condition. During the accuracy tests, the CFL number is decreased in order to maintain the stability of the SSP Runge-Kutta solver.

**Example 3.1.** *The primary objective of the initial test scenario is to validate whether the method effectively preserves the exact C-property in the presence of an uneven bottom configuration. We examine two distinct functions to represent the characteristics of the bottom topography, denoted as $z(x)$, where $x$ lies in the interval $[0, 10]$. The first function is given by:*

$$z(x) = 5 \exp(-\frac{2}{5}(x - 5)^2). \tag{16}$$

*This function is smooth and continuous. The second function is defined as:*

$$z(x) = \begin{cases} 4 & x \in [4,8], \\ 0 & otherwise, \end{cases} \tag{17}$$

*This function is discontinuous, having a constant value of* 4 *within the interval* $[4,8]$*, and being zero elsewhere. The initial condition is determined by the stationary solution (the stationary solution refers to the particular solution that remains constant over time), which satisfies the following conditions:*

$$h + z = 10, \qquad hv = 0.$$

*It is imperative to maintain the exact preservation of this steady state. Using a uniform mesh containing* 400 *points, we compute the solution up to a time of* $t = 0.5$*. Simple transmissive boundary conditions were applied. Fig. 1 illustrates the graphical representation of the determined water surface level* $h+z$ *and the bottom elevation* $z$ *for Eq. (16). To verify the preservation of the exact C-property within round-off error, we performed calculations utilizing three different levels of precision: single, double, and quadruple. The tables 1 and 2 display the corresponding* $L_1$ *and* $L_\infty$ *errors for both the water height* $h$ *and the discharge* $hv$ *for the two bottom functions (16) and (17) across various precisions. The observations from the tables indicate that the extent of round-off errors across different precisions closely correlates with the magnitude of the* $L_1$ *and* $L_\infty$ *errors. This outcome serves as strong evidence supporting the preservation of the exact C-property.*

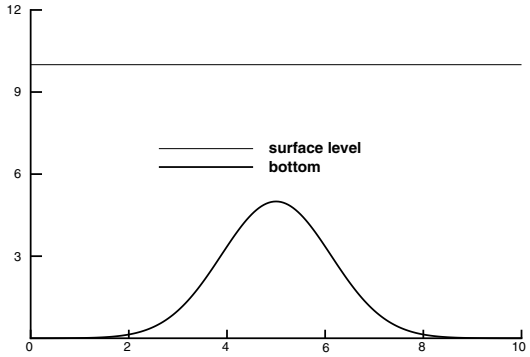


Figure 1: The $h + z$ and $z$ for Example 3.1 at the final time $t = 0.5$ $s$.

Table 1: Errors with different norms for the stationary solution with initial condition (16)

| | $h$ | | $hv$ | |
|---|---|---|---|---|
| precision | $L_1$ error | $L_\infty$ error | $L_1$ error | $L_\infty$ error |
| single | 1.19(-6) | 7.65(-6) | 1.17(-5) | 2.67(-5) |
| double | 1.09(-12) | 5.54(-12) | 1.87(-11) | 9.23(-12) |
| quadruple | 1.18(-25) | 5.17(-25) | 3.34(-23) | 9.45(-24) |

Table 2: Errors with different norms for the stationary solution with initial condition (17)

| | $h$ | | $hv$ | |
|---|---|---|---|---|
| precision | $L_1$ error | $L_\infty$ error | $L_1$ error | $L_\infty$ error |
| single | 1.44(-6) | 2.05(-6) | 2.87(-6) | 1.67(-6) |
| double | 2.45(-13) | 3.24(-13) | 2.36(-12) | 4.58(-12) |
| quadruple | 2.27(-25) | 4.80(-26) | 1.78(-25) | 3.21(-25) |

**Example 3.2.** *In this instance, we will evaluate the effectiveness of our method in accurately representing a smooth solution by examining its fourth-order accuracy. Therefore, we have decided to utilize the profile of the sea-floor or land surface and initial functions as follow:*

$$z(x) = \sin^2(\pi x), \qquad h(x,0) = 5 + \exp(\cos(2\pi x)), \qquad (hv)(x,0) = \sin(\cos(2\pi x)), \qquad x \in [0,1].$$

*These conditions are accompanied by periodic boundary conditions. Since the precise solution is unknown for this specific scenario, a comparative solution was derived by employing the identical fourth-order central-upwind method, albeit with a more extensive grid consisting of* $30,000$ *points. This reference solution is then considered as the "exact" solution for the purpose of computing numerical errors in comparison to the other solutions. The computations are performed up to a time of* $t = 0.1$ *since, at this point, the solution remains smooth without any significant distortions or irregularities. The errors and their respective numerical orders of accuracy are provided in Table 3. It is evident that this example achieves fourth-order accuracy, as indicated by the results in the table.*

Table 3: Errors and numerical orders of accuracy for the example 3.2

| | discharge ($hv$) | | | | water height ($h$) | | | |
|---|---|---|---|---|---|---|---|---|
| N | $L_1$-error | $L_1$-order | $L_\infty$-error | $L_\infty$-order | $L_1$-error | $L_1$-order | $L_\infty$-error | $L_\infty$-order |
| 20 | 7.99(-3) | — | 5.21(-3) | — | 5.64(-3) | — | 3.35(-3) | — |
| 40 | 2.83(-4) | 4.81 | 2.01(-4) | 4.69 | 1.82(-4) | 4.95 | 1.26(-4) | 4.73 |
| 80 | 1.14(-5) | 4.63 | 7.12(-6) | 4.81 | 6.86(-6) | 4.73 | 4.29(-6) | 4.88 |
| 160 | 6.46(-7) | 4.14 | 4.21(-7) | 4.07 | 4.13(-7) | 4.05 | 2.58(-7) | 4.05 |
| 320 | 3.66(-8) | 4.14 | 2.60(-8) | 4.01 | 2.13(-8) | 4.27 | 1.33(-8) | 4.28 |
| 640 | 2.17(-9) | 4.07 | 1.47(-9) | 4.14 | 1.42(-9) | 3.90 | 8.44(-10) | 3.99 |
| 1280 | 1.28(-10) | 4.08 | 8.00(-11) | 4.20 | 8.55(-11) | 4.05 | 4.83(-11) | 4.13 |

**Example 3.3.** *The subsequent test scenario, which remains almost stationary, was initially suggested by LeVeque in the publication [16]. The purpose behind selecting this specific test case was to demonstrate the capability of the developed method in handling calculations that involve a rapidly changing flow over a smooth bed, along with perturbations to a stationary state. The configuration of the land or sea-floor in this case is characterized by a single hump, defined by the following equation:*

$$z(x) = \begin{cases} 0.25(\cos(10\pi(x-1.5))+1) & x \in [1.4, 1.6], \\ 0 & \textit{otherwise.} \end{cases} \tag{18}$$

*The initial conditions for the problem are defined as follows:*

$$(hv)(x,0) = 0, \qquad h(x,0) = \begin{cases} 1 - z(x) + \varepsilon & x \in [1.1, 1.2], \\ 1 - z(x) & \textit{otherwise.} \end{cases} \tag{19}$$

*In Eq. (19), the initial values of the height and velocity are specified. The velocity component is set to zero initially, while the height component is determined based on the position* $x$*. Within the interval* $[1.1, 1.2]$*, the height is given by* $1 - z(x) + \varepsilon$*, where* $\varepsilon$ *represents a non-zero perturbation constant. Outside this interval, the height is* $1 - z(x)$*. Two scenarios have been simulated: one with* $\varepsilon = 0.2$ *(representing a large pulse) and another with* $\varepsilon = 0.001$ *(representing a little pulse). In a theoretical sense, when* $\varepsilon$ *is tiny, the disturbance is expected to split into two waves that propagate in opposite directions at characteristic speeds of* $\pm\sqrt{gh}$*. Numerical methods often encounter challenges when dealing with calculations that involve minor fluctuations or disturbances occurring on the surface of the water, as noted by LeVeque in [16]. The solutions at a time of* $t = 0.2$ *s for both the scenarios involving a large pulse and a small pulse were calculated using a uniform grid consisting of* $200$ *cells (grid points). Simple transmissive boundary conditions were applied. Additionally, a comparison was made with a solution obtained using a grid with* $N = 5000$ *cells. The results are depicted in Fig. 2. It is evident from the results displayed in Fig. 2 that there are no spurious numerical oscillations present. This observation confirms the essential non-oscillatory nature of the new central-upwind method employed in the computations.*

**Example 3.4.** *In this instance, we replicate the scenario of a dam breaking over a raised rectangular surface, resulting in a swiftly changing water flow across an uneven terrain. This particular case study was employed in [21]. The equation provided below describes the arrangement or shape of the sea floor or ocean floor:*

$$z(x) = \begin{cases} 8 & |x - 750| \le 1500/8, \\ 0 & \textit{otherwise.} \end{cases} \tag{20}$$

*These conditions are applicable to values of* $x$ *ranging from* $0$ *to* $1500$*. Simple transmissive boundary conditions were applied. The initial functions for the shallow water equations are described as follows: for the function* $(hv)(x,0)$*, its initial value is* $0$ *for all values of* $x$*. For the function* $h(x,0)$*, its initial value depends on the location* $x$*: when*

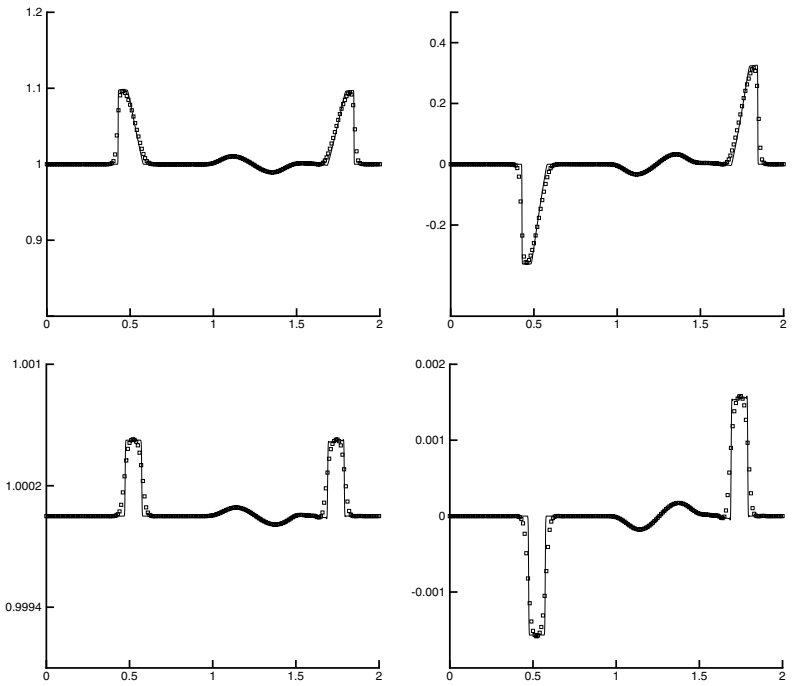


Figure 2: Numerical and reference solutions for the surface level $h + z$ (left) and the discharge $hv$ (right). Small perturbation of a steady-state water with a big pulse (top) and a small pulse (bottom) (Example 3.3) at the final time $t = 0.2$ $s$. The solid line is "reference solution" and □ is "numerical solution".

*$x$ is less than or equal to 750, the initial value of $h(x, 0)$ is equal to 20 minus the depth $z(x)$, otherwise, the initial value of $h(x, 0)$ is equal to 15 minus the depth $z(x)$.*

*The computational results generated using $N = 500$ uniformly distributed points (along with a comparison to the results obtained using $N = 10,000$ uniformly distributed points) are illustrated in Fig. 3. The figure displays the results for two distinct time durations: $t = 15$ $s$ and $t = 60$ $s$. Please refer to Fig. 3 for visualization. The employed scheme demonstrates excellent performance in this particular example, providing finely resolved and non-oscillatory solutions when using $N = 500$ points. These solutions are in agreement with the converged results obtained using $N = 10,000$ points.*

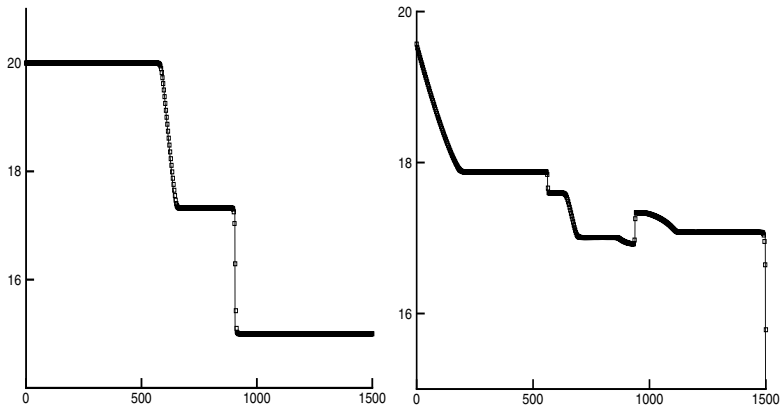


Figure 3: Numerical and reference solutions for the surface level $h + z$ of the dam breaking problem (Example 3.4) at the final time $t = 15$ $s$ (left) and $t = 60$ $s$ (right). The solid line is "reference solution" and □ is "numerical solution".

**Example 3.5.** *The example mentioned in [7] utilized an almost exact solution, which was a highly accurate approximation derived asymptotically. We employ this example to conduct additional testing and evaluation of our method. The function $z(x)$, representing the bottom profile, is defined as follows:*

$$z(x) = 10 + \frac{40x}{L} + 10\sin\left(\pi\left(\frac{4x}{L} - \frac{1}{2}\right)\right), \tag{21}$$

*where $L = 14000\ m$ denotes the channel length. By considering the following initial and boundary conditions:*

$$h(x,0) = 60.5 - z(x), \quad (hv)(x,0) = 0,$$
$$h(0,t) = 64.5 - 4\sin\left(\pi\left(\frac{4t}{86400} + \frac{1}{2}\right)\right), \quad (hv)(L,t) = 0,$$

*we can derive a remarkably precise approximate solution using asymptotic analysis:*

$$h(x,t) = 64.5 - z(x) - 4\sin\left(\pi(\frac{4t}{86400} + \frac{1}{2})\right),$$

*and*

$$(hv)(x,t) = \frac{(x-L)\pi}{5400}\cos\left(\pi(\frac{4t}{86400} + \frac{1}{2})\right).$$

*We utilize a uniform spatial resolution of $\Delta x = 70m$. Fig. 4 demonstrates a side-by-side evaluation of the computational results and the theoretical solutions at a specific time instant of $t = 7552.13s$. The level of concurrence between them is highly satisfactory.*

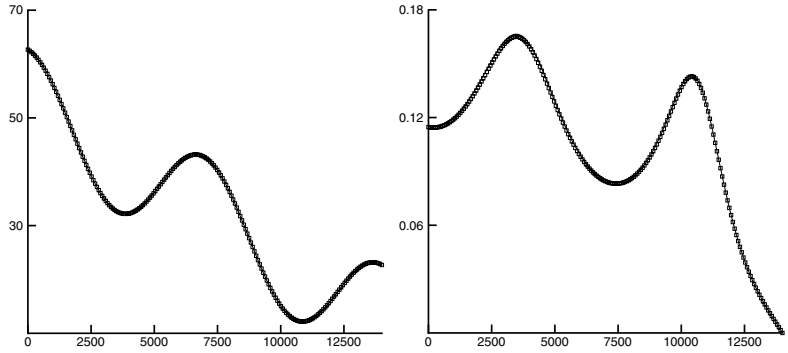


Figure 4: Numerical and analytic solutions for the tidal wave flow (Example 3.5) at the final time $t = 7552.13\ s$. The solid line is "analytic solution" and □ is "numerical solution". Left: water height $h$; right: velocity $v$.

## 4. Concluding remarks

This paper presented an expansion of the high-order central-upwind methods, enabling their application to solve the shallow water system in a single spatial dimension. By employing a approach to handle the source terms, we can create tailored approximations that ensure the central-upwind methods exhibit precise C-property for motionless stationary solutions involving water. Furthermore, these techniques maintain their inherent high-order accuracy and exhibit predominantly non-oscillatory behaviour in a broad sense. The developed numerical scheme is illustrated through a multitude of numerical instances, demonstrating its ability to accurately and efficiently resolve shocks without introducing oscillations. These examples highlight the scheme's precise adherence to the C-property in the field of shallow water equations.

## Acknowledgements

The author is very thankful to the reviewers for carefully reading the paper, their comments and suggestions have improved the quality of the paper.

## References

[1] R. Abedian, *High-order semi-discrete central-upwind schemes with Lax-Wendroff-type time discretizations for Hamilton-Jacobi equations*, Comput. Methods Appl. Math., 18 (2018), pp. 559–580.

[2] ——, *A new high-order weighted essentially non-oscillatory scheme for non-linear degenerate parabolic equations*, Numer. Methods Partial Differential Equations, 37 (2021), pp. 1317–1343.

[3] ——, *A finite difference Hermite RBF-WENO scheme for hyperbolic conservation laws*, Internat. J. Numer. Methods Fluids, 94 (2022), pp. 583–607.

[4] ——, *A modified high-order symmetrical WENO scheme for hyperbolic conservation laws*, Int. J. Nonlinear Sci. Numer. Simul., 24 (2023), pp. 1521–1538.

[5] R. Abedian and M. Dehghan, *The formulation of finite difference RBFWENO schemes for hyperbolic conservation laws: an alternative technique*, Adv. Appl. Math. Mech., 15 (2023), pp. 1023–1055.

[6] E. Audusse, M.-O. Bristeau, and B. Perthame, *Kinetic schemes for Saint-Venant equations with source terms on unstructured grids*, Research Report RR-3989, INRIA, 2000. Projet M3N.

[7] A. Bermudez and M. E. Vazquez, *Upwind methods for hyperbolic conservation laws with source terms*, Comput. & Fluids, 23 (1994), pp. 1049–1071.

[8] K. O. Friedrichs and P. D. Lax, *Systems of conservation equations with a convex extension*, Proc. Nat. Acad. Sci. U.S.A., 68 (1971), pp. 1686–1688.

[9] T. Gallouët, J.-M. Hérard, and N. Seguin, *Some approximate Godunov schemes to compute shallow-water equations with topography*, Comput. & Fluids, 32 (2003), pp. 479–513.

[10] A. Kurganov and D. Levy, *A third-order semidiscrete central scheme for conservation laws and convection-diffusion equations*, SIAM J. Sci. Comput., 22 (2000), pp. 1461–1488.

[11] ——, *Central-upwind schemes for the Saint-Venant system*, M2AN Math. Model. Numer. Anal., 36 (2002), pp. 397–425.

[12] A. Kurganov, S. Noelle, and G. Petrova, *Semidiscrete central-upwind schemes for hyperbolic conservation laws and hamilton–jacobi equations*, SIAM J. Sci. Comput., 23 (2001), pp. 707–740.

[13] A. Kurganov and G. Petrova, *Central schemes and contact discontinuities*, M2AN Math. Model. Numer. Anal., 34 (2000), pp. 1259–1275.

[14] ——, *A third-order semi-discrete genuinely multidimensional central scheme for hyperbolic conservation laws and related problems*, Numer. Math., 88 (2001), pp. 683–729.

[15] A. Kurganov and E. Tadmor, *New high-resolution central schemes for nonlinear conservation laws and convection-diffusion equations*, J. Comput. Phys., 160 (2000), pp. 241–282.

[16] R. J. LeVeque, *Balancing source terms and flux gradients in high-resolution Godunov methods: the quasi-steady wave-propagation algorithm*, J. Comput. Phys., 146 (1998), pp. 346–365.

[17] H. Nessyahu and E. Tadmor, *Non-oscillatory central differencing for hyperbolic conservation laws*, J. Comput. Phys., 87 (1990), pp. 408–463.

[18] S. Rathan, N. R. Gande, and A. A. Bhise, *Simple smoothness indicator WENO-Z scheme for hyperbolic conservation laws*, Appl. Numer. Math., 157 (2020), pp. 255–275.

[19] S. Rathan and G. Naga Raju, *A modified fifth-order WENO scheme for hyperbolic conservation laws*, Comput. Math. Appl., 75 (2018), pp. 1531–1549.

[20] C.-W. Shu and S. Osher, *Efficient implementation of essentially non-oscillatory shock-capturing schemes*, J. Comput. Phys., 77 (1988), pp. 439–471.

[21] S. Vukovic and L. Sopta, *ENO and WENO schemes with the exact conservation property for one-dimensional shallow water equations*, J. Comput. Phys., 179 (2002), pp. 593–621.

[22] Z. Zhao, Y. Chen, and J. Qiu, *A hybrid Hermite WENO scheme for hyperbolic conservation laws*, J. Comput. Phys., 405 (2020), pp. 109175, 22.

[23] Z. Zhao and J. Qiu, *A Hermite WENO scheme with artificial linear weights for hyperbolic conservation laws*, J. Comput. Phys., 417 (2020), pp. 109583, 23.

Please cite this article using:

Rooholah Abedian, A new central-upwind scheme for solving the shallow water equations, AUT J. Math. Comput., 6(3) (2025) 193-203
https://doi.org/10.22060/AJMC.2023.22640.1182